

Electrochemical impedance spectroscopic characterization on nano-sized $\text{Ca}_3\text{Co}_3\text{FeO}_9$ electrode with enhanced capacity retention

Young-Dae Ko · Jin-Gu Kang · Jae-Gwan Park · Dong-Wan Kim

Received: 5 March 2009 / Accepted: 16 August 2009 / Published online: 27 August 2009
© Springer Science+Business Media B.V. 2009

Abstract A $\text{Ca}_3\text{Co}_3\text{FeO}_9$ electrode exhibiting enhanced cycle-life performance compared to that of Co_3O_4 was presented in this study. In order to examine the mechanism of the improved capacity retention in the $\text{Ca}_3\text{Co}_3\text{FeO}_9$ electrode, the cycling-induced variation of electrode kinetics was observed using electrochemical impedance spectroscopy. The separable electrochemical reactions using the appropriate equivalent circuit and the goodness-of-fit results demonstrated the superior charge-transfer kinetics of $\text{Ca}_3\text{Co}_3\text{FeO}_9$, compared to Co_3O_4 , during prolonged cycling. These results clearly demonstrated the benefits of the inactive CaO matrix that is spontaneously formed in $\text{Ca}_3\text{Co}_3\text{FeO}_9$ during the first discharge process.

Keywords $\text{Ca}_3\text{Co}_3\text{FeO}_9$ · Li-ion batteries · Capacity retention · Electrochemical impedance spectroscopy · Charge-transfer kinetics

1 Introduction

In the last decade, advances in the electrode materials of rechargeable lithium-ion batteries have been the main

avenues for improving electrochemical performance in terms of high power density, high energy density, and long-term cycle stability. Carbon, a commercialized anode material with low theoretical capacity (392 mA h g^{-1}), presents a barrier for further application in mobile electronic devices and hybrid electric vehicles that require high capacity with stable capacity retention [1]. Thus, numerous studies have been performed to exploit novel anode alternatives, especially focusing on the nanostructuring of materials [2–4] to meet industrial demands.

In particular, nano-sized Co_3O_4 has attracted much attention since Poizot et al. suggested a new electrochemical lithiation/delithiation mechanism, called conversion reaction which differs from the classic lithium intercalation/deintercalation and alloying/dealloying processes [5]. The conversion reaction is understood by the complete reduction of Co_3O_4 to nanograin Co metal domains embedded in the electrochemically reversible amorphous Li_2O matrix ($\text{Co}_3\text{O}_4 + 8\text{Li} \rightleftharpoons 3\text{Co} + 4\text{Li}_2\text{O}$). In spite of the high theoretical capacity (892 mA h g^{-1}) of Co_3O_4 , as deduced by the conversion mechanism which delivers eight electrons during electrochemical reactions, it suffers from deteriorated cycling performance [6, 7] that prohibits practical applications. Large volume expansion can induce electrical segregation of electrochemically active components (Co and Li_2O), eventually leading to capacity fading upon prolonged cycling [8].

Owing to the significance of capacity retention, diverse approaches such as one-dimensional nanowire Co_3O_4 [9], nanostructured thin film Co_3O_4 [10], and $\text{Co}_3\text{O}_4/\text{C}$ nanocomposite [11] have been investigated extensively to achieve long-term cycle stability. Another approach is the formation of the active–inactive nanocomposites, in which the inactive matrix acts as a buffer to relieve the strain associated with the volume changes and prevent the

Young-Dae Ko and Jin-Gu Kang contributed equally to this work.

Y.-D. Ko · J.-G. Kang · J.-G. Park
Nano-materials Research Center, Nano-science Research
Division, Korea Institute of Science and Technology,
Seoul 136-791, Korea

D.-W. Kim (✉)
Department of Materials Science and Engineering,
Ajou University, Suwon 443-749, Korea
e-mail: dwkim@ajou.ac.kr

aggregation of the active nano regions [12, 13]. Recently, we reported that $\text{Ca}_3\text{Co}_4\text{O}_9$ exhibited an electrochemical conversion reaction into nanograin Co metal surrounded by a Li_2O matrix, thereby inducing a sustained cycling performance due to the self-formation (during the first discharge) of an electrochemically inactive CaO matrix ($\text{Ca}_3\text{Co}_4\text{O}_9 + 12\text{Li} \rightarrow 3\text{CaO} + 4\text{Co} + 6\text{Li}_2\text{O}$) [14]. Although the inactive CaO matrix may play a key role in enhancing capacity retention, few studies have reported its role in detail. To obtain a deeper insight into the beneficial effects of the inactive CaO matrix on cycling characteristics, further experimental analysis is required.

In the present study, we examine the origin of capacity retention and the effect of the CaO matrix in $\text{Ca}_3\text{Co}_3\text{FeO}_9$ electrodes (analogous to $\text{Ca}_3\text{Co}_4\text{O}_9$), in comparison with Co_3O_4 nanopowders, by observing the simultaneous variation in electrochemical impedance spectroscopy (EIS) upon cycling. By fitting experimental data with an equivalent circuit analog, we quantitatively analyze the electrochemical kinetic processes. Based on the trend in charge-transfer kinetics as a function of cycle number, a feasible model for capacity retention in $\text{Ca}_3\text{Co}_3\text{FeO}_9$ is proposed and discussed.

2 Experimental

Nano-sized $\text{Ca}_3\text{Co}_3\text{FeO}_9$ and Co_3O_4 particles were prepared via the citrate-gel method. The detailed synthetic procedures are discussed elsewhere [14]. The electrochemical characterization of $\text{Ca}_3\text{Co}_3\text{FeO}_9$ and Co_3O_4 nanopowders was carried out using Swagelok-type two electrode half cells. The positive electrodes were prepared by mixing active material (1–2 mg of $\text{Ca}_3\text{Co}_3\text{FeO}_9$ or Co_3O_4 powder) with 20 wt% Super P carbon black (MMM Carbon, Brussels, Belgium), 13 wt% Kynar 2801 binder (PVdF-HFP) and 1-methyl-2-pyrrolidionone (NMP) solvent. The resulting slurry was cast onto a Cu foil current collector and dried in a vacuum oven at 100 °C. Lithium metal foil was employed as a negative electrode and Celgard 2400 film as a separator. The electrolytic solution was composed of 1 M LiPF_6 dissolved in a 1:1 volume ratio of ethylene carbonate to dimethyl carbonate. The cells were assembled in an Ar-filled glove box to block air and moisture.

Galvanostatic cycling characteristics were measured in the voltage window of 0.01–3.0 V by means of an automatic battery cycler (WBCS 3000, WonATech, Korea). EIS measurements were carried out at room temperature using an electrochemical test unit (Solartron 1260, UK). Initially, the assembled half cell with an open circuit voltage of ~ 3.0 V was galvanostatically (1C) discharged to 0.01 V, after which the impedance response was

collected by applying 5 mV amplitude ac voltage while maintaining a constant dc voltage (0.01 V) in the sweeping frequency range of 1 MHz–1 mHz. Subsequently, galvanostatic charging was conducted until 3.0 V, followed by the same ac measurement as in the previous discharged case. These steps were reiterated at the 5th, 10th, 50th and 100th cycles. The obtained impedance spectra were analyzed quantitatively by curve fitting with Z-view software (Version. 2.90, Scribner Associates Inc.).

3 Results and discussion

Galvanostatic voltage profiles of Co_3O_4 - and $\text{Ca}_3\text{Co}_3\text{FeO}_9$ -based half cells at a rate of 0.2C are depicted in Fig. 1a, b, respectively. The transmission electron microscopy (TEM) images (Fig. 1 insets) indicate that both powders were composed of 10–30 nm-sized nanoparticles. The Co_3O_4 and $\text{Ca}_3\text{Co}_3\text{FeO}_9$ nanoparticles had large surface areas of 30.3 and 39.2 $\text{m}^2 \text{g}^{-1}$, respectively, as measured by the Brunauer–Emmett–Teller method. The voltage-capacity curves of the Co_3O_4 nanoparticles were similar to those previously reported [8]. The first discharge and charge capacities were 1,237 and 835 mA h g^{-1} , respectively.

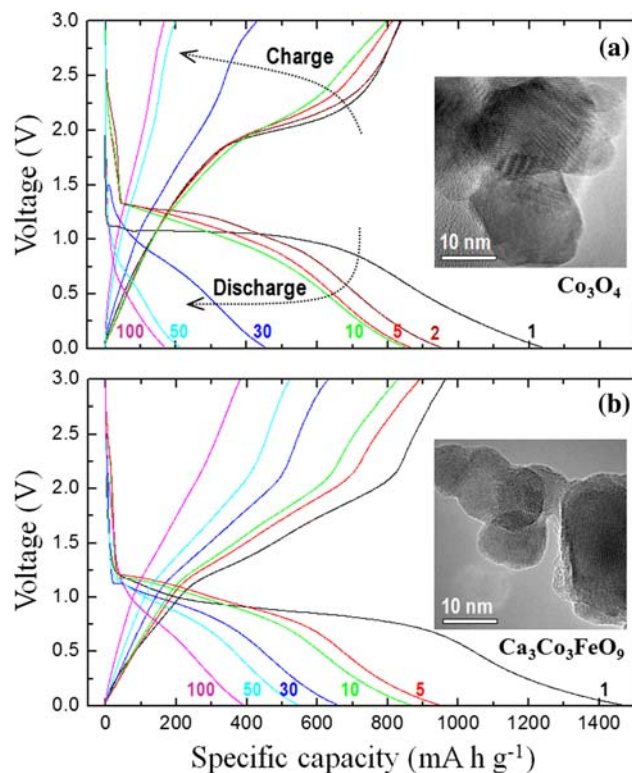


Fig. 1 Galvanostatic discharge/charge voltage profiles of nano-sized **a** Co_3O_4 and **b** $\text{Ca}_3\text{Co}_3\text{FeO}_9$ electrodes at a rate of 0.2C in the voltage window of 0.01–3.0 V. The inset shows the typical TEM images of each powder

The extra capacity that was present during the first discharge process was attributed to the formation of a solid electrolyte interface (SEI) layer [5]. However, the electrochemical cycling capacity of the nano-sized Co_3O_4 remained stable over the subsequent cycles until the 10th cycle, and was maintained close to its theoretical capacity of $890.4 \text{ mA h g}^{-1}$, but then decreased significantly to ~ 454 and 211 mA h g^{-1} after 30 and 50 cycles, respectively, suggesting a drastic loss in the electrochemical activity for the Co_3O_4 electrode. The capacity of the $\text{Ca}_3\text{Co}_3\text{FeO}_9$ nanoparticles was similar to that of Co_3O_4 at the 10th cycle, but then decreased to 546 mA h g^{-1} after 50 cycles, demonstrating the much better capacity retention of the $\text{Ca}_3\text{Co}_3\text{FeO}_9$ nanoparticles compared to the Co_3O_4 nanoparticles. As previously reported for $\text{Ca}_3\text{Co}_4\text{O}_9$, the superior capacity retention of the $\text{Ca}_3\text{Co}_3\text{FeO}_9$ nanoparticles is closely related to the formation of an inactive matrix due to the new electrochemical conversion reaction ($\text{Ca}_3\text{Co}_3\text{FeO}_9 \rightleftharpoons 3\text{CaO} + 3\text{Co} + \text{Fe} + 6\text{Li}_2\text{O}$) [14]. This inactive CaO matrix can alleviate the mechanical stress induced by the volume variation of the active regions and prevent localized aggregation of the Co or Fe nanodomains upon cycling, thereby improving the capacity retention.

To provide a deeper insight into the origin of the capacity retention in $\text{Ca}_3\text{Co}_3\text{FeO}_9$ nanoparticles, EIS analysis was conducted for the $\text{Ca}_3\text{Co}_3\text{FeO}_9/\text{Li}$ half cell. EIS is a powerful tool to investigate electrochemical systems because of its effective separation of several electrochemical processes with distinguishable relaxation times. Therefore, an analysis of the impedance behavior can provide distinctive information on the contribution of lithium ion migration in the SEI layers, charge-transfer kinetics at the electrode/electrolyte interface, electronic conduction through composite electrodes, and the solid-state diffusion of lithium ions. In general, electrochemical processes during the lithiation and delithiation of electrode materials can be interpreted by an equivalent electrical circuit that combines resistive and capacitive components. The equivalent circuit demonstrated in Fig. 2a can therefore be applied to analyze the impedance responses of $\text{Ca}_3\text{Co}_3\text{FeO}_9$ - and Co_3O_4 -based electrodes. As can be seen, an equivalent circuit is made up of a serial connection of (i) R_{el} , (ii) $R_{sei} \parallel \text{CPE}_{sei}$ (CPE_{sei} parallel to R_{sei}), (iii) $R_{ct} \parallel \text{CPE}_{dl}$, (iv) $R_b \parallel \text{CPE}_b$, and (v) W_o , where R_i denotes the resistance of each component and CPE_i (Constant Phase Element) the capacitance instead of pure capacitance (C) in order to reflect the non-homogeneous nature of the porous composite electrode, resulting in the depressed semicircular shape [13, 15]. W_o is indicative of the finite length Warburg diffusion contribution, including the transition to capacitive behavior.

Figure 2b exhibits a typical Nyquist plot for the 10th discharged state of the $\text{Ca}_3\text{Co}_3\text{FeO}_9$ electrode as representative, where the overall frequency range is divided into

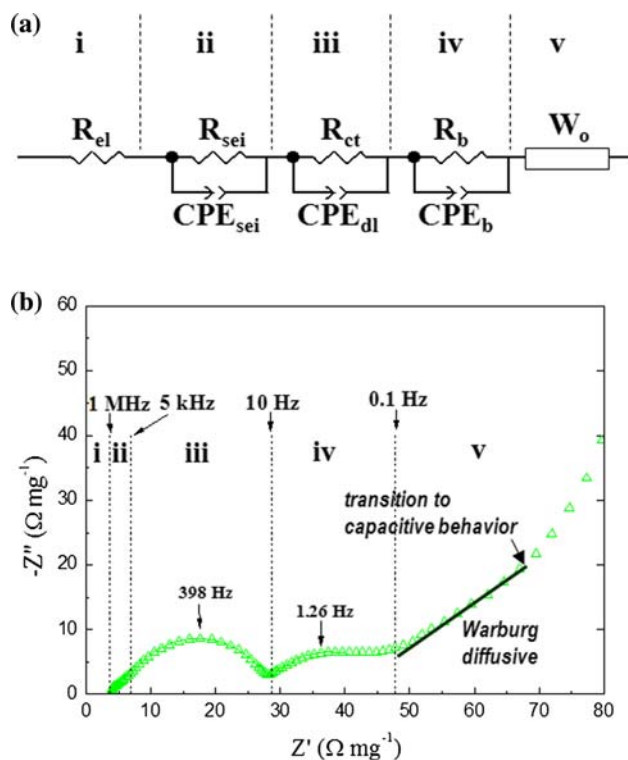


Fig. 2 a An equivalent circuit analog for representing several electrochemical processes and for curve fitting. b A representative Nyquist plot of the $\text{Ca}_3\text{Co}_3\text{FeO}_9/\text{Li}$ half cell at the 10th discharged state and a 1C rate for dividing the overall frequency range into an individual frequency range corresponding to each kinetic process

five individual sections (i–v) corresponding to respective electrochemical processes, as described in Fig. 2a. The Z' -axis intercept (R_{el}) in section i represents the ionic resistance of the electrolyte, and two overlapped semicircular arcs in the high frequency range (1 MHz–10 Hz) indicate the lithium ionic conduction through the SEI layers (ii) and the charge-transfer reaction at the electrode/electrolyte interface (iii) [16]. A depressed semicircle in the intermediate frequency range (10–0.1 Hz) is related to the electronic transport through the bulk composite electrodes (iv), followed by one linear region inclined to the Z' -axis with a specific slope (lower than 45°), implying lithium ion Warburg diffusion into the solid-state medium, and another linear region with a steeper slope accounting for the capacitive behavior (v) in the low frequency range (0.1 Hz–1 MHz) [16]. This capacitive trend originates from the limited diffusion path and reflective boundary condition because the composite electrode consists of nano-sized particulates that easily accumulate charge carriers [17]. The proposed equivalent circuit analog and discussion about the sectioning of the Nyquist plot can also be applied to the Co_3O_4 -based system.

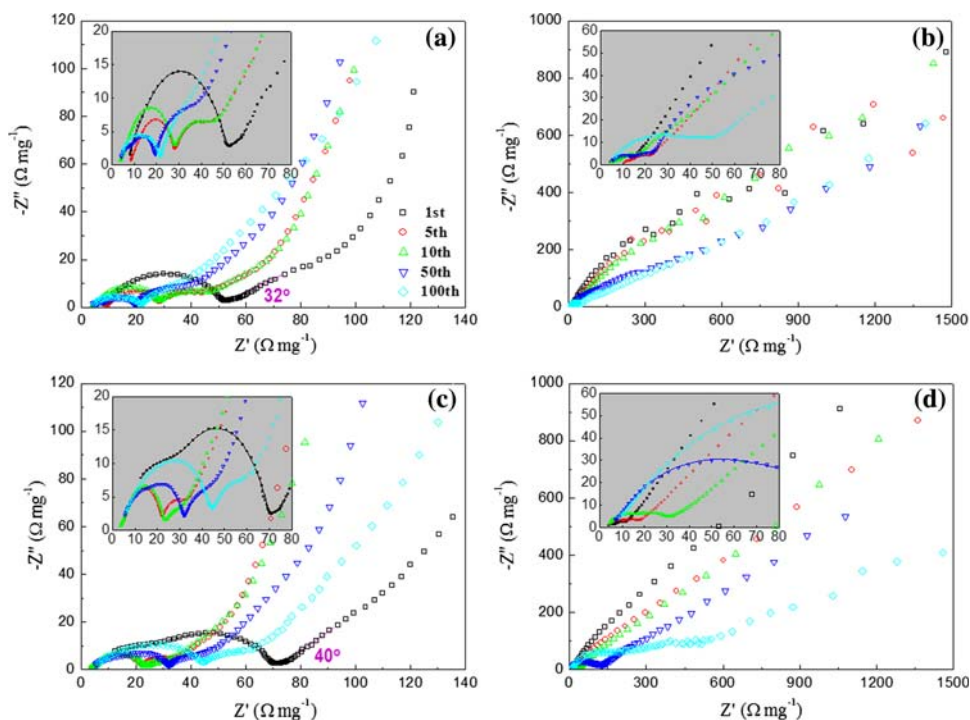
The family of Nyquist plots of the discharged and charged states at the 1st, 5th, 10th, 50th, and 100th cycles

for both $\text{Ca}_3\text{Co}_3\text{FeO}_9$ and Co_3O_4 electrodes are represented in Fig. 3a–d. The inset of each figure provides a magnified view, including two overlapped depressed semicircles and one depressed semicircle for the spectra in the high-to-intermediate frequency range. Figure 3b, d shows the merging of two overlapped arcs into one large depressed semicircle with continuous cycling, which was attributed to the inseparable relaxation time constants that were induced by the considerably increased resistance of the SEI layers and the charge-transfer reaction. Comparing the intermediate frequency region of Fig. 3a with that of Fig. 3b, the impedance spectra of the charged states exhibited much larger bulk resistance (R_b) than the discharged states, which was attributed to the fact that the nanodomain Co and Fe metals with high electrical conductivity existed in a discharged state, whereas the oxidized transition metals (CoO and Fe_3O_4) with low conductivity formed in a charged state. The same comparison is also made in the Co_3O_4 nanopowder, as identified in Fig. 3c, d. A typical Warburg impedance inclined at 45° to the Z' -axis in the Nyquist plot accounts for the lithium ion diffusion through the homogeneous single phase [18]. However, the slopes of the Warburg diffusive region of the first discharged states in Fig. 3a, c were 32° and 40° , respectively, which slightly deviated from typical Warburg characteristics. In general, lower than typical Warburg slopes appear owing to the existence of a phase boundary in the two-phase regions, porosity or inhomogeneity in the structure [19]. Over the low frequency region in the $\text{Ca}_3\text{Co}_3\text{FeO}_9$ and Co_3O_4 discharged states (Fig. 3a, c), a capacitive trend was clearly

observed at all cycles. On the other hand, the capacitive behaviors in the charged states of both materials were masked by bulk resistance semicircles and Warburg diffusive responses due to the excessively sluggish kinetics of electronic transport through the bulk composite and the solid-state lithium ion diffusion.

For the quantitative analysis, values of the circuit elements were deduced by fitting (chi-square, χ^2 in the magnitude of 10^{-4} to 10^{-5}) the Nyquist plots in Fig. 3a–d with an equivalent circuit analog (Fig. 2a). Because of either insufficient development of spectra in the low frequency range or the existence of indistinctive relaxation times among kinetic processes, fitting was implemented over the restricted frequency ranges, i.e., a high-to-intermediate range in the discharged states and a high range in the charged ones. Figure 4 shows the variation of the calculated intrinsic resistances at both discharged and charged states as a function of the cycle number. R_{el} values for $\text{Ca}_3\text{Co}_3\text{FeO}_9$ and Co_3O_4 seldom dropped below $10 \Omega \text{ mg}^{-1}$, even after 100 cycles, implying that the electrochemical cells were operating under stable states when measured (Fig. 4a). However, the difference in the variation of R_{sei} according to the cycle number is worth discussing for both samples, as shown in Fig. 4b. The much lower R_{sei} of $\text{Ca}_3\text{Co}_3\text{FeO}_9$ than that of Co_3O_4 at the first discharged state demonstrated the ability of $\text{Ca}_3\text{Co}_3\text{FeO}_9$ to stabilize the surface film during the initial period. R_{sei} of Co_3O_4 in the discharged state decreased from the first to fifth cycle, due to the activation of the surface film [20]. In both discharged and charged cases, R_{sei} of Co_3O_4 was higher

Fig. 3 Family of Nyquist plots collected from the 1st, 5th, 10th, 50th, and 100th discharged and charged states of the $\text{Ca}_3\text{Co}_3\text{FeO}_9$ and Co_3O_4 electrodes: **a** discharged and **b** charged states of the $\text{Ca}_3\text{Co}_3\text{FeO}_9$ electrode, and **c** discharged and **d** charged states of the Co_3O_4 electrode. The inset of each figure presents a magnified view of the high-to-intermediate frequency ranges



and increased more rapidly than that of $\text{Ca}_3\text{Co}_3\text{FeO}_9$, especially in the charged state. It is believed that the evolution and growth of the SEI layer or surface film exhibited various effects on the electrode performance. In particular, the continuous growth of the surface film on the electrode destroyed the surface film, thereby deteriorating the electrode kinetics and cell performances [21].

More importantly, Fig. 4c represents the significant difference in the variation of R_{ct} according to cycle number for both electrode materials in the discharged and charged states. The R_{ct} values of the discharged states were drastically reduced in the initial period for the two electrodes due to the activation of the electrode surface for charge transfer with the onset of current flux [22]. The discrepancy of R_{ct} between the two electrodes exhibited a clear trend as a function of cycle number. While R_{ct} of Co_3O_4

continuously increased without any disturbance that of $\text{Ca}_3\text{Co}_3\text{FeO}_9$ was maintained almost constant from the 50th to 100th iterations after the initial 10th cycle. For the charged states, Co_3O_4 exhibited a dramatic increase of R_{ct} values as the cycling proceeded whereas R_{ct} showed only a negligible increase (almost constant in comparison with Co_3O_4), even during prolonged cycling. The considerably lower R_{ct} values of $\text{Ca}_3\text{Co}_3\text{FeO}_9$ compared to those of Co_3O_4 until the 100th cycle in both the discharged and charged cases indicated the facile charge-transfer kinetics at the $\text{Ca}_3\text{Co}_3\text{FeO}_9$ electrode/electrolyte interface. The charge-transfer reaction can be enhanced by activating the electrode surface, which is related to the active mass exposed to the electrolyte and the change in the surface layer thickness owing to the current flux [22, 23]. During the initial periods, both $\text{Ca}_3\text{Co}_3\text{FeO}_9$ and Co_3O_4 were capable of supplying a sufficient amount of electrochemically active part composed of nano-sized transition metal oxides, nanograin Co, or Fe metal embedded in the Li_2O matrix [14]. However, after prolonged discharge/charge cycling of Co_3O_4 , nanograin aggregation occurred, leading to the separation of nanograin Co metal from Li_2O matrix. As a result, nanodomains with inhomogeneous composition were widely distributed in the particles, where the formation of Co_3O_4 during the charge process was energetically unfavorable. This reduced the active mass at the electrode surface and caused the sluggish charge transfer. On the other hand, the inactive CaO matrix as a ‘spectator’ in the $\text{Ca}_3\text{Co}_3\text{FeO}_9$ nanocomposite enabled the effective mitigation of nanograin aggregation and prevented the occurrence of internal cracking by accommodating the strain upon subsequent cycles. Consequently, the charge-transfer resistance of $\text{Ca}_3\text{Co}_3\text{FeO}_9$ was appreciably suppressed as a function of cycle number.

The electrochemical cycling feature is mainly determined by several kinetic processes occurring on the electrode materials, such as lithium ion transport through the surface film, electronic conduction inside the bulk composite, charge transfer at the interface, and solid-state diffusion. Although each individual factor has its own effect on cycle performance, we can select that which best describes both the drastic capacity decay of Co_3O_4 and the stable capacity retention of $\text{Ca}_3\text{Co}_3\text{FeO}_9$. According to Shaju et al. [22], electrical isolation of the active mass (related to R_b) is unlikely to be the main origin of capacity fading because the liquid electrolyte provides the predominant path for charge carriers. Thus, we can exclude the possible effect of bulk composite resistance on cycle retention. This negligible impact of R_b on cycling features was experimentally supported by comparing the R_b values of $\text{Ca}_3\text{Co}_3\text{FeO}_9$ with Co_3O_4 electrodes, as depicted in Fig. 4d. The R_b value of the $\text{Ca}_3\text{Co}_3\text{FeO}_9$ electrode consistently increased while maintaining a higher level than that of the Co_3O_4 electrode, the

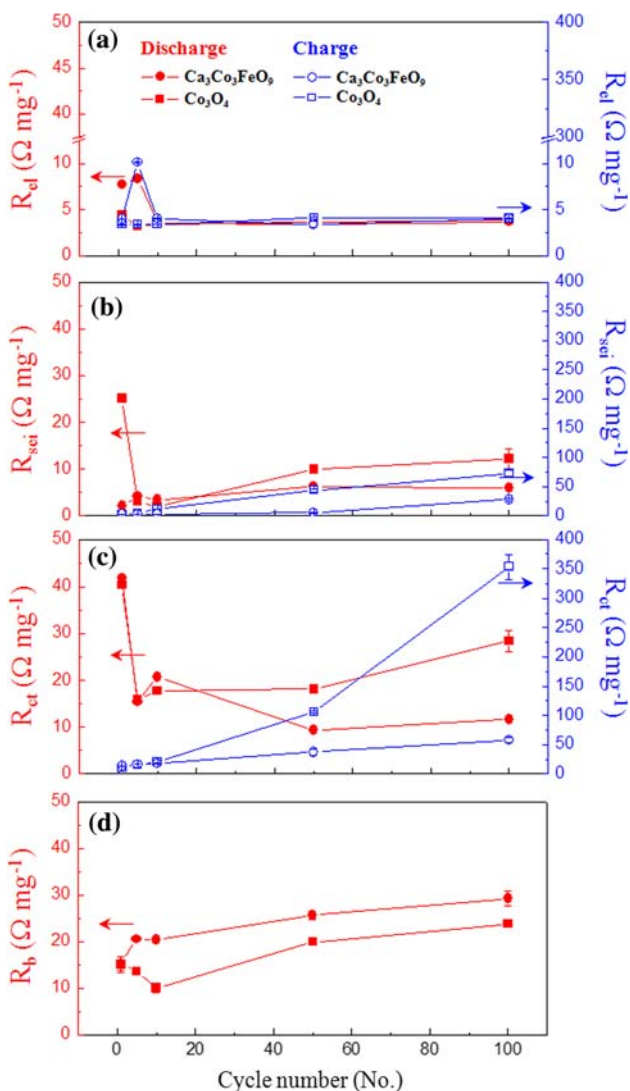


Fig. 4 Variation of the calculated intrinsic resistances at the discharged and charged states versus the cycle number for the $\text{Ca}_3\text{Co}_3\text{FeO}_9$ and Co_3O_4 electrodes. **a** R_{el} , **b** R_{sei} , **c** R_{ct} , and **d** R_b

behavior of which was contradictory to the improved cycle stability of the former. The transformation of both materials to a similar phase such as metallic nanograin (discharged state) or transition metal oxides (charged state) suggested a negligible difference in solid-state lithium ion diffusion between the two electrodes. Furthermore, Co_3O_4 , which suffered from drastic capacity decay, showed considerably larger R_{ct} values (charged: $354 \pm 20 \Omega \text{ mg}^{-1}$, discharged: $28 \pm 2 \Omega \text{ mg}^{-1}$) than R_{sci} ones (charged: $72 \pm 5 \Omega \text{ mg}^{-1}$, discharged: $12 \pm 2 \Omega \text{ mg}^{-1}$), indicating that charge-transfer kinetics played a crucial role in the electrode kinetics and cycling performance. We, therefore, concluded that the mitigation of nanograin aggregation by inactive CaO matrix maintained the facile charge-transfer kinetics up to 100 cycles and stabilized the cycle performance.

4 Conclusion

We used EIS analysis to reveal the direct association between the superior capacity retention of $\text{Ca}_3\text{Co}_3\text{FeO}_9$ electrodes and their charge-transfer kinetics. Having excluded other possible reasons for the cycle performance discrepancies between the $\text{Ca}_3\text{Co}_3\text{FeO}_9$ and Co_3O_4 electrodes, we focused on the charge-transfer phenomena in this study. The charge-transfer reaction is crucially determined by the amount of the electro-active part exposed to the liquid electrolyte. This electro-active part, such as the nanograin Co and Fe surrounded by a Li_2O matrix in the discharged states or transition metal oxides in the charge states, generally aggregates after numerous cycles. For the Co_3O_4 electrodes, therefore, the inhomogeneous nanodomains, which cannot proceed with further discharge/charge cycling, take over most of the nanoparticle and consequently reduce the active part for efficient charge-transfer kinetics. In the presence of an inactive CaO matrix in the $\text{Ca}_3\text{Co}_3\text{FeO}_9$ electrodes, however, CaO exerts a beneficial effect on the charge-transfer kinetics by mitigating the nanograin aggregation and internal cracking. Therefore, the $\text{Ca}_3\text{Co}_3\text{FeO}_9$ electrodes in the present study showed appreciably lower R_{ct} values than Co_3O_4 as a function of cycle number, leading to stable cycle characteristics. We expect the present study results will provide further insight

into the charge-transfer kinetics and enable the electrode materials to be tailored with superior capacity retention.

Acknowledgments This work was supported by the National Research Foundation of Korea (NRF) grant funded by the Korea government (MEST) (No. 2009-0082544).

References

- Whittingham MS (2008) MRS Bull 33:411
- Arico AS, Bruce P, Scrosati B, Tarascon JM, Schalkwijk WV (2005) Nat Mater 4:366
- Lee DH, Park JG, Choi KJ, Choi HJ, Kim DW (2008) Eur J Inorg Chem 6:878
- Jiang C, Hosono E, Zhou H (2006) Nanotoday 1:28
- Poizot P, Laruelle S, Grugeon S, Dupont L, Tarascon JM (2000) Nature 407:496
- Shaju KM, Jiao F, Debart A, Bruce PG (2007) Phys Chem Chem Phys 9:1837
- Grugeon S, Laruelle S, Dupont L, Tarascon JM (2003) Solid State Sci 5:895
- Larcher D, Sudant G, Leriche JB, Chabre Y, Tarascon JM (2002) J Electrochem Soc 149:A234
- Nam KT, Kim DW, Yoo PJ, Chiang CY, Meethong N, Hammond PT, Chiang YM, Belcher AM (2006) Science 312:885
- Chou SL, Wang JZ, Liu HK, Dou SX (2008) J Power Sources 182:359
- Needham SA, Wang GX, Konstantinov K, Tournayre Y, Lao Z, Liu HK (2006) Electrochem Solid State Lett 9:A315
- Sharma N, Shaju KM, Rao GVS, Chowdari BVR (2004) Electrochim Acta 49:1035
- Sharma N, Rao GVS, Chowdari BVR (2005) Electrochim Acta 50:5305
- Kim DW, Ko YD, Park JG, Kim BK (2007) Angew Chem Int Ed 46:6654
- Yu P, Ritter JA, White RE, Popov BN (2000) J Electrochem Soc 147:2081
- Sharma N, Plevart J, Rao GVS, Chowdari BVR, White TJ (2005) Chem Mater 17:4700
- Levi MD, Aurbach D (2004) J Phys Chem B 108:11693
- Reddy MV, Madhavi S, Rao GVS, Chowdari BVR (2006) J Power Sources 162:1312
- Shaju KM, Rao GVS, Chowdari BVR (2004) J Electrochem Soc 151:A1324
- Shaju KM, Rao GVS, Chowdari BVR (2003) J Mater Chem 13:106
- Christensen J, Newman J (2004) J Electrochem Soc 151:A1977
- Shaju KM, Rao GVS, Chowdari BVR (2003) J Electrochem Soc 150:A1
- Levi MD, Gamolsky K, Aurbach D, Heider U, Oesten R (2000) Electrochim Acta 45:1781